CHAPTER 3

EXPERIMENTAL PROCEDURES

This chapter describes all the experimental procedures employed in this work. It is appropriate to discuss the various experimental aspects of thin films preparation and characterization. Surface characterization was done by using an AFM and SEM. The thin film thickness was determined from the cross-section SEM images. The energy gap, structural properties were investigated by UV–vis spectroscopy and XRD and Raman spectroscopy. Electrical properties were measured using gold coated as electrical contacts. Optical properties of the films were characterized using ionolominescence. Moreover, photocatalytic activities were studied using the absorption spectra of methylene blue under the sun light irradiation.

3.1 Chemical substances

3.1.1 Zinc wire (∅ 0.38 mm, 99.97% purity, Advance Research Material LTD)

3.1.2 Zinc plate (5 × 5 × 0.62 mm, 99.9% purity, Alfa Aesar®)

3.1.3 Titanium wire ((∅ 0.25 mm, 99.5% purity, Advance Research Material LTD)

3.1.4 Quartz (12.7 × 12.7 × 1.0 mm^3, Ted Pella, Inc., Redding, CA)

3.1.5 N_2

3.1.6 Argon

3.1.7 O_2

3.1.8 Purify air

3.1.9 KOH

3.1.10 Ethanol

3.1.11 Methylene blue

3.1.12 Acetone

3.1.13 Trichoroethylene

3.1.14 Distilled water

3.2 Instruments

3.2.1 Power Supply

3.2.2 Optical microscope (MXT-α7, MEIJO, Japan)

3.2.3 Capacitor 0.1 μF

3.2.4 Capacitor 0.035 μF

3.2.5 Vertical sliding wire holder

3.2.6 Horizontal wire holder

3.2.7 Ohm meter

3.2.8 Venire Calliper

3.2.9 Quartz cutter

3.2.10 Beaker

3.2.11 Pliers

3.2.12 Furnace

3.2.13 Gold coated glass

3.2.14 Dropper

3.2.15 Vacuum chamber and 10^{-6} torr pump

3.2.16 Function generator (Tektronic CFG 250)

3.2.17 High voltage power supply/Amplifier/Controller (Trek 610E)

3.2.18 Oscilloscope (Tektronic 2225)

3.2.19 Ultrasonic cleaner (Mettler Electronics)

3.3 Sample preparation

3.3.1 Vertical tip alignment capacitor discharge sparking

For study effect of tip shape and voltage on the size of nanoparticles (NPs), the zinc tips were vertically aligned. Before the NPs were formed on quartz substrates by the high voltage discharge (sparking) through the zinc tip, the substrates were sonically cleaned in acetone, ethanol and distilled water, and dried in blowing nitrogen gas. Different tip shapes were prepared from the zinc wire by three methods: (i) electrochemical etching for the conical tip; in brief the zinc wire was partially dipped into a 2.5 M KOH solution and was anodically dissolved at 6 volts (fig. 3.1(a)), (ii) cutting with pliers for a sharp tip (fig. 3.1(b)) and (iii) polishing with an abrasive paper for the dull tip(fig. 3.1 (c)).

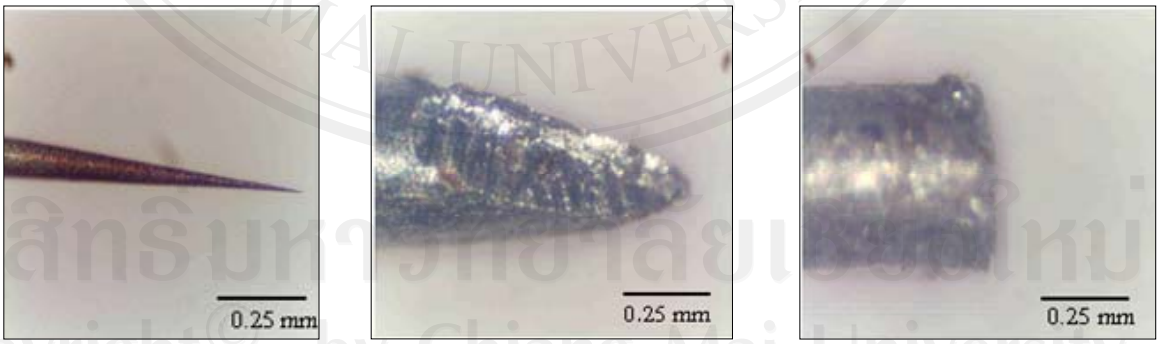

Fig. 3.1 Optical microscope images of (a) the conical tip, (b) the sharp tip and (c) the dull tip.

The prepared tip was then placed vertically at 3 mm above another zinc wire which was placed horizontally on the quartz substrate (fig. 3.2). After a 0.1 μF capacitor was charged to the desired voltages (2, 4 and 6 kV), the tip was gradually moved downward to the substrate until sparking occurred in ambient air at atmospheric pressure.

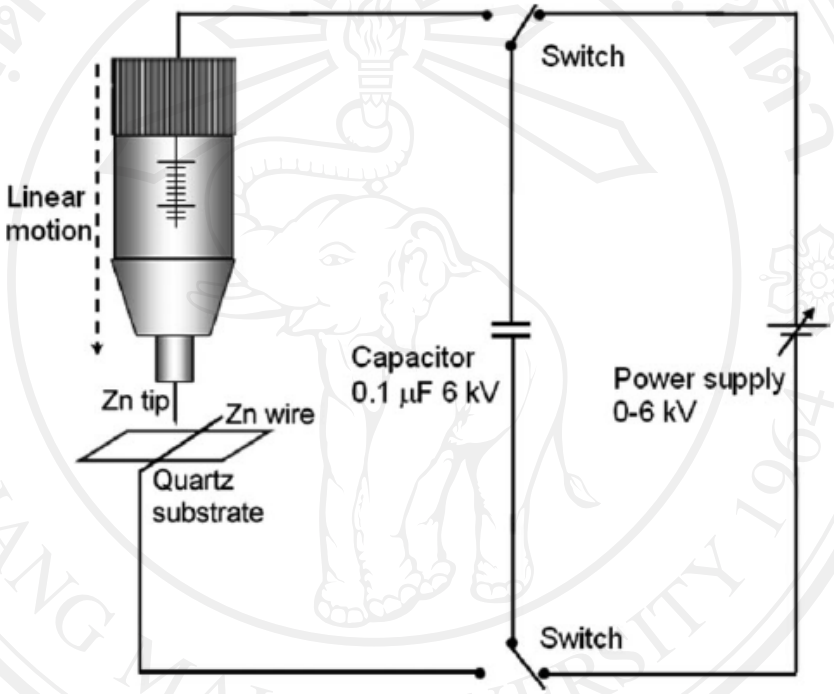

Fig. 3.2 Schematic diagram of vertical tip alignment sparking**. [**50**]**

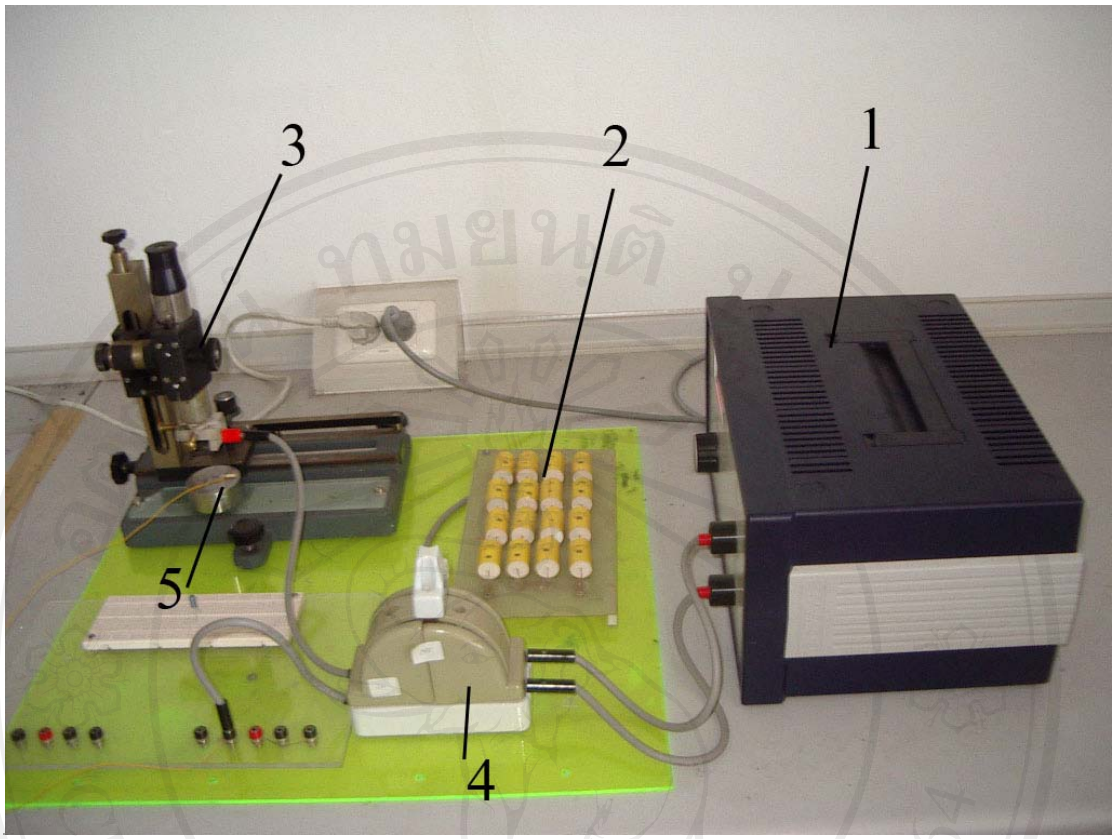

Fig. 3.3 Capacitor discharge sparking apparatus: 1 Power supply, 2 Capacitor 0.1 μF, 3 vertical slider, 4 Switch and 5 substrate base.

3.3.2 Horizontal tip alignment capacitor discharge sparking

(1) ZnO nanoparticles thin films

Sparking process is the process for depositing zinc oxide nanoparticles on quartz substrates. The sparking process of two zinc tips was shown schematically in fig. 3.4 and experimental apparatus in fig. 3.5. The quartz substrates were sonically cleaned in acetone, ethanol, and distilled water, and then dried in nitrogen gas blowing. The two sharp tips were prepared from the zinc wire. The tips were then placed horizontally at 3 mm apart and 2 mm above the center of the substrate.

The sparking occurred when the capacitor was charged to 10 kV and connected to the two tips by the rotating switch. The experiment was done repeatedly 50-200 times in ambient air at atmospheric pressure with the sparking time of 3 sec/spark. The as-deposited films were pre-annealed at 380 °C for 1 h and then annealed at 400-800 °C for another 1 h. Moreover, effects of the sparking pressure on the size of nanoparticle were studied under pressure 160-760 torr.

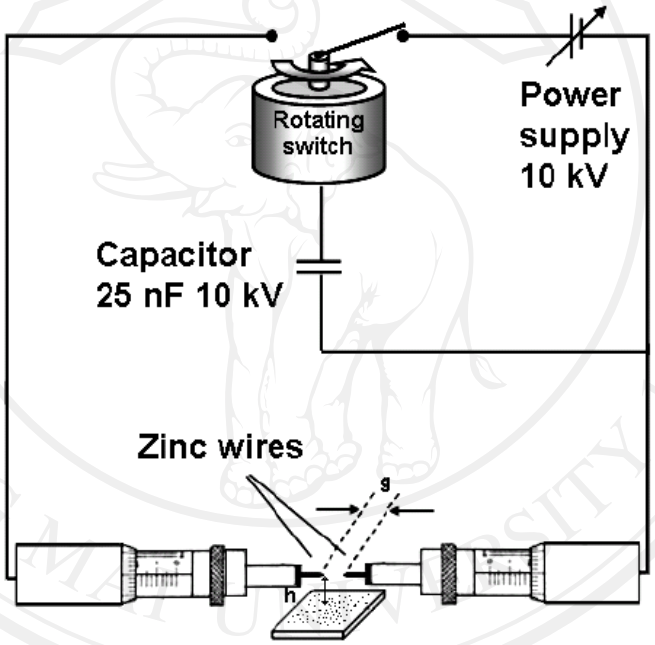

Fig. 3.4 Schematic diagram of the double tip sparking apparatus. [51]

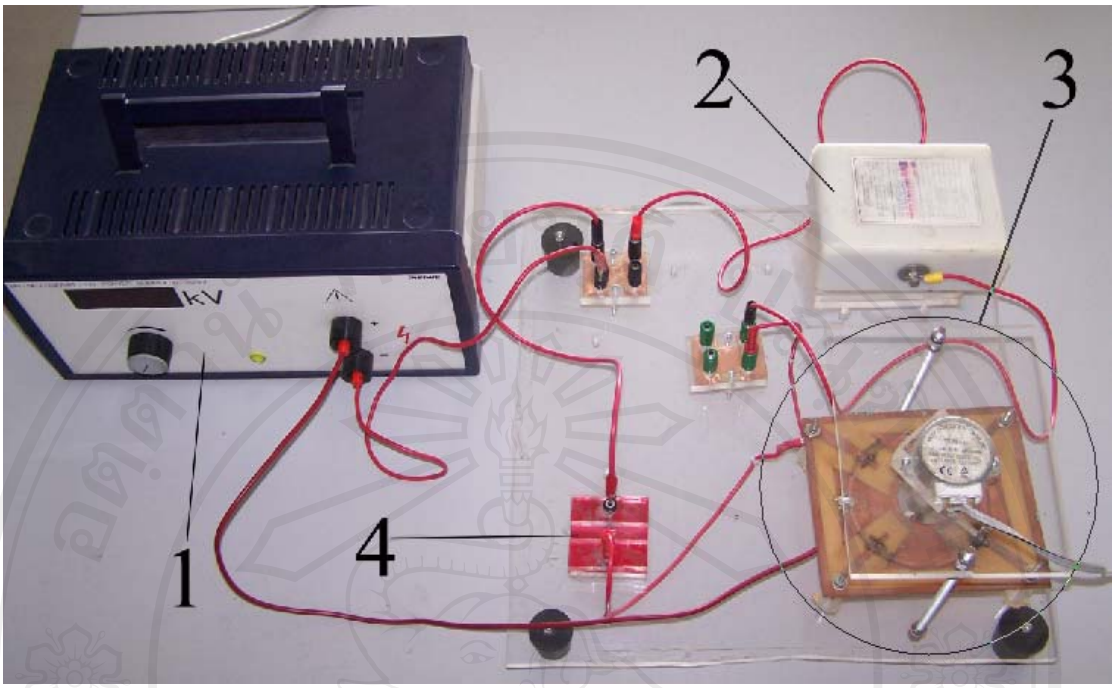

Fig. 3.5 Capacitor discharge sparking apparatus: 1 Power supply, 2 Capacitor 0.035 μF, 3 Switch, and 4 substrate.

(2) ZnO-TiO_2 coupled nanoparticle thin films

High voltage (10 kV), discharge form capacitor, was applied over the two sharp tips, Titanium wire and Zinc wire. The experimental apparatus is the same of the ZnO thin films which shown in fig. 3.4 and fig. 3.5. The quartz substrates, sonically cleaned in acetone, ethanol, and distilled water, and then dried by nitrogen gas blowing. The tips were then placed horizontally at 3 mm apart and 2 mm above the center of the substrate. The metal wires were alternated as anode and cathode. The experiment was done in air atmospheric pressure at room temperature with the sparked repeatedly, 3 s/spark. The ZnO-TiO_2 films were annealed at 600 °C for 1 h.

3.3.3 Square wave pulse sparking

The sparking method for depositing ZnO thin films on zinc substrate was depicted schematic diagram in fig. 3.6 and experimental apparatus in fig 3.7. The zinc substrates were sonically cleaned in trichlorothylene, acetone, methanol and distilled water for 15 minutes, and then dried in nitrogen gas blowing. The two sharp tips, prepared from the zinc wires, were placed horizontally at 3 mm apart and 2 mm above the center of the substrate. The pure air, without humidity, was blown into the in vacuum chamber. The sparking occurred when the 10 kV 50% duty cycle 100 Hz square wave was applied over the tips. The experiment was done for 2 hours. The samples were then annealed in air at 200-350 °C for 30 minutes.

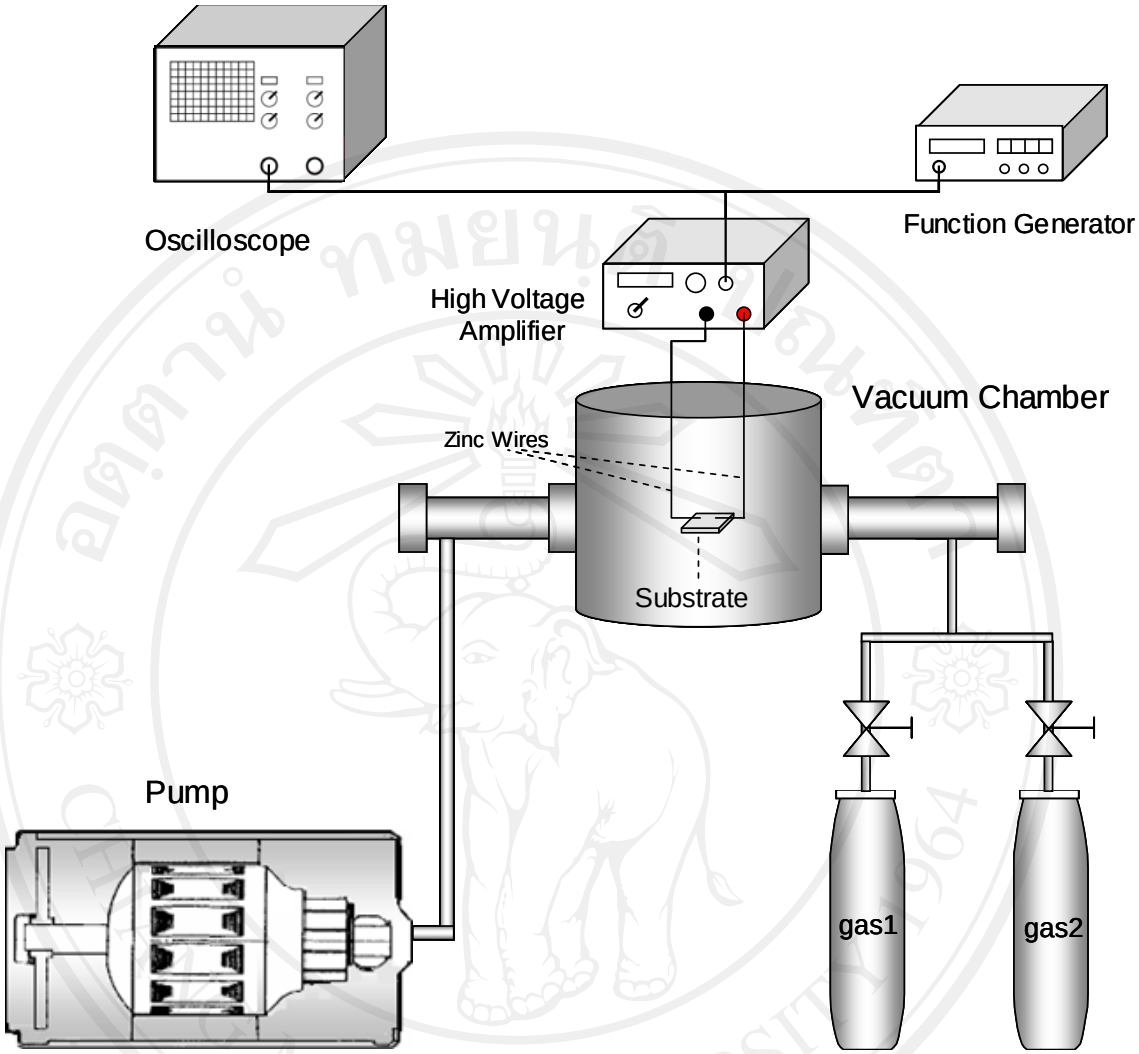

Fig. 3.6 Schematic diagram of square wave pulse sparking.

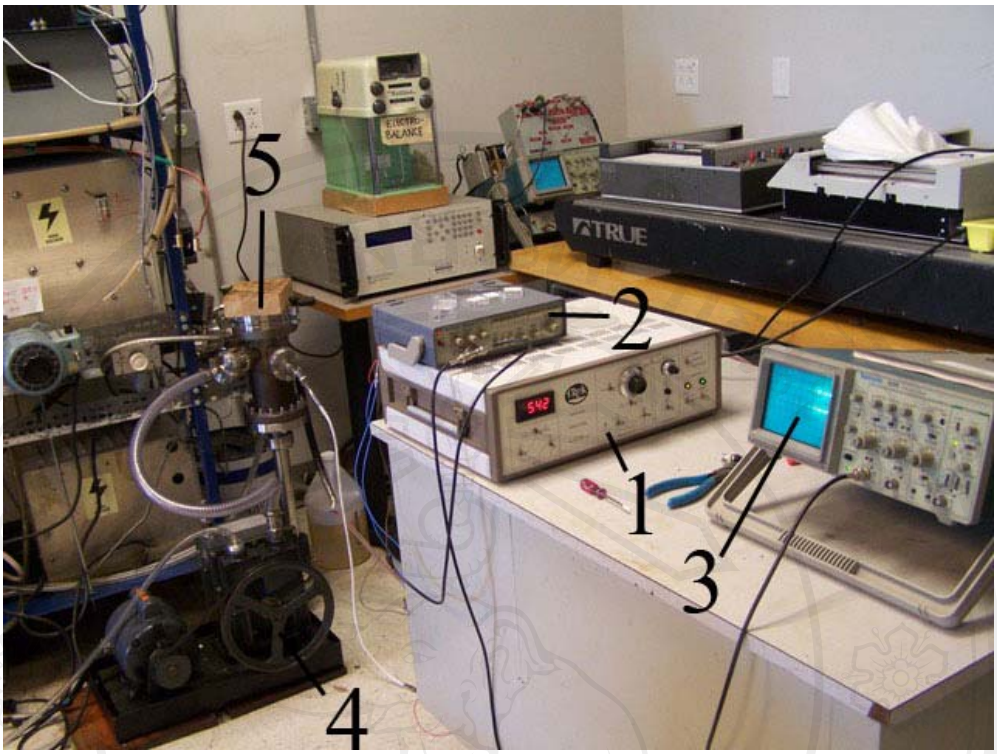

Fig. 3.7 Square wave pulse sparking apparatus: 1 voltage amplifier, 2 function generator, 3 oscilloscope, 4 pump and 5 vacuum chamber.

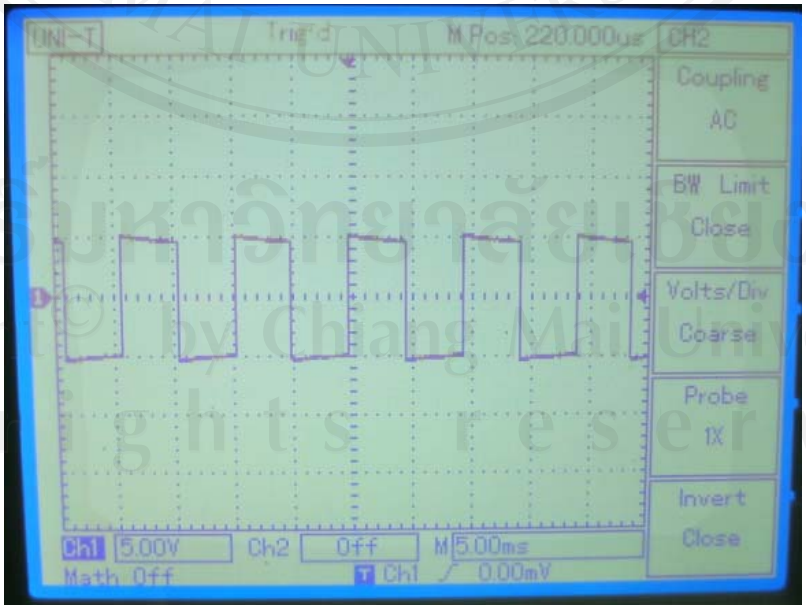

Fig. 3.8 Square wave pulse of 100 Hz, 50% duty cycle.

3.4 Sample characterization

3.4.1 Atomic force microscope (AFM)

Atomic force microscopy (AFM) is a method of measuring surface morphology on a scale from angstroms to 100 microns. The technique involves imaging a sample through the use of a probe or tip. The tip is positioned at the end of a cantilever beam shape. As the tip is repelled by or attracted to the surface, the cantilever beam deflects. The magnitude of the deflection is captured by a laser that reflects at an oblique angle from the very end of the cantilever. A plot of the laser deflection versus tip position on the sample surface provides the resolution of the hills and valleys that constitute the topography, the topography of an area is also the description of such surface shapes and features, of the surface.

In addition to basic AFM, the instrument is capable of producing images in a number of other modes, including tapping, magnetic force, electrical force, and pulsed force. In tapping mode, the tip is oscillated above the sample surface, and data may be collected from interactions with surface topography, stiffness, and adhesion. These results in an expanded number of image contrast methods compared to basic AFM. Magnetic force mode imaging utilizes a magnetic tip to enable the visualization of magnetic domains on the sample. In electrical force mode imaging a charged tip is used to locate and record variations in surface charge. In pulsed force mode, the sample is oscillated beneath the tip, and a series of pseudo force-distance curves are generated. This permits the separation of sample topography, stiffness, and adhesion values, producing three individual images simultaneously.

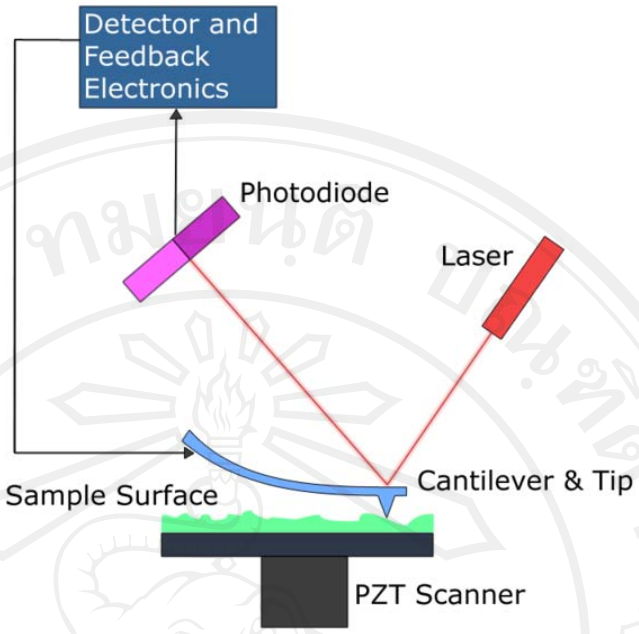

Fig. 3.9 Principle of the AFM [52]

In this work, surface morphology and root-mean-square (rms) roughness of the samples were characterized by Atomic Force Microscope (AFM, Digital Instruments, Inc., Santa Barbara, CA) using the tapping mode. Section analysis was carried out to estimate roughness of thin films and sizes of the nanoparticles using the Nanoscope IIIa 5.12r3 software which are shown in fig. 3.10 and 3.11.

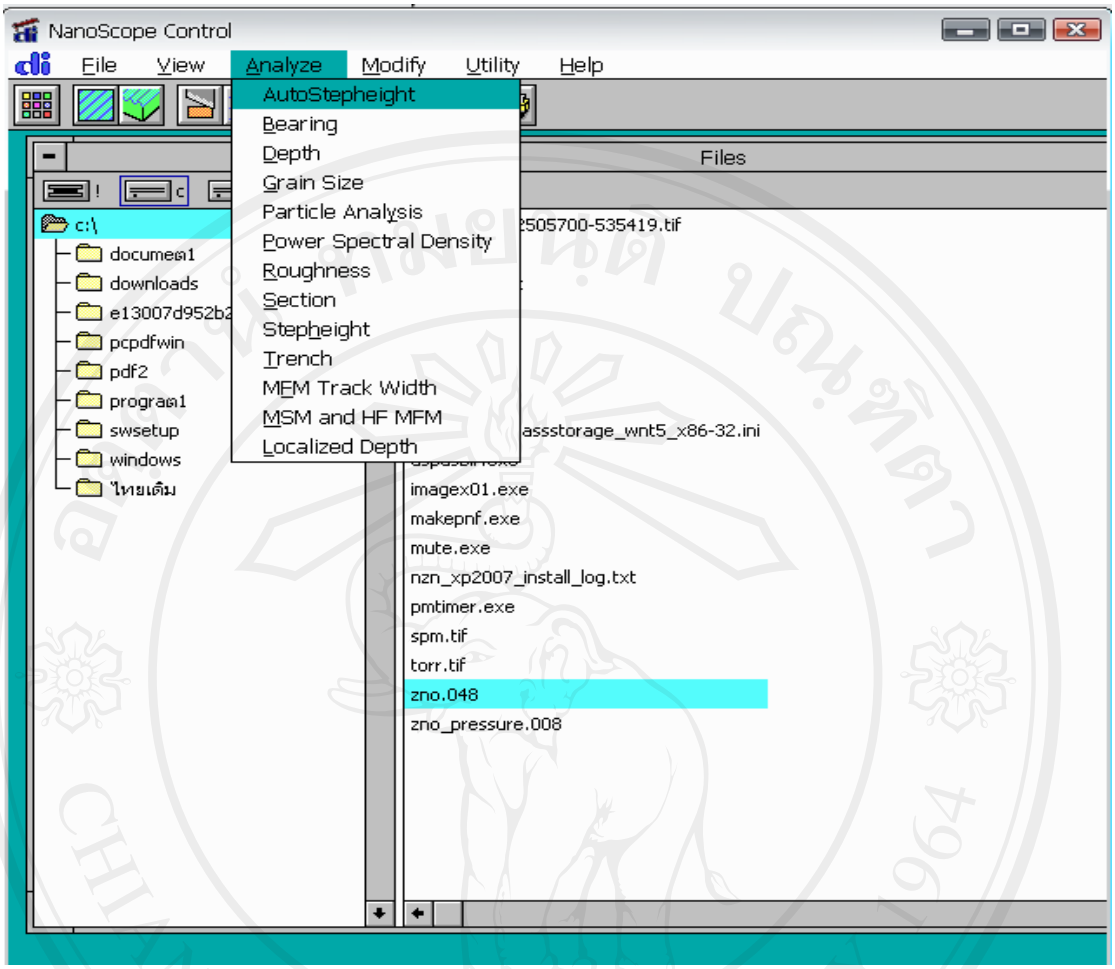

Fig. 3.10 Nanoscope IIIa 5.12r3 software.

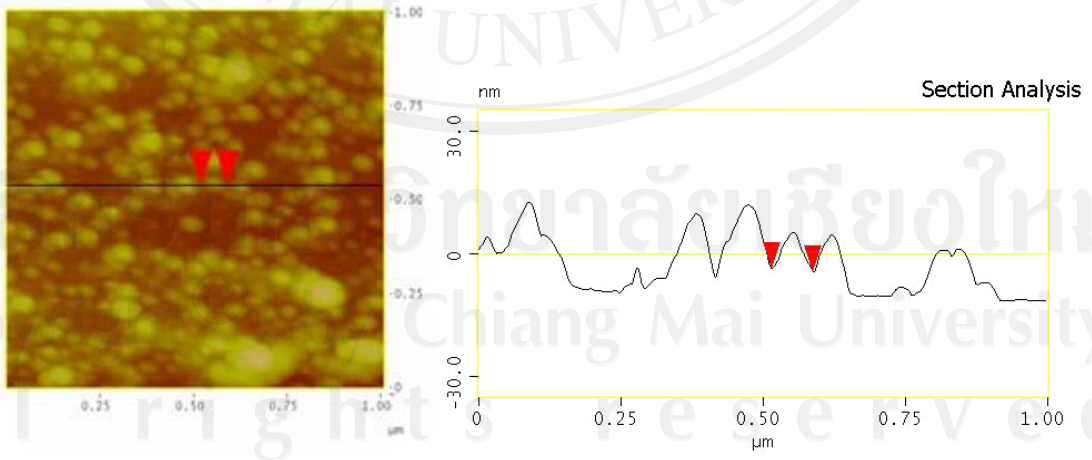

Fig. 3.11 Nanoscope IIIa 5.12r3 software for estimate the height and diameter of the nanoparticles.

Fig. 3.12 Atomic Force Microscope

3.4.2 Scanning electron microscope (SEM)

The SEM is a microscope that uses electrons instead of light to form an image. A beam of electrons is produced at the top of the microscope by an electron gun. The electron beam follows a vertical path through the microscope, which is held within a vacuum. The beam travels through electromagnetic fields and lenses, which focuses the beam down toward the sample.

When the primary electron beam interacts with the sample, the electrons lose energy by scattering and absorption within the interaction volume. The size of the interaction volume depends on the electron's landing energy, the atomic number of the specimen and the specimen's density. The energy exchanged between the electron beam and the sample results in the reflection of high-energy electrons by elastic scattering, emission of secondary electrons by inelastic scattering and the emission of electromagnetic radiation, where each of which can be detected by specialized

detectors. The beam current absorbed by the specimen can also be detected and used to create images.

A JEOL JSM 6335F as shown in fig. 3.13 was used to determine surface morphology and thickness of the films. The electron source is cold cathode field emission. The films were coated with gold sputtering for 30 second.

Fig. 3.13 Field Emission Scanning Electron Microscope

3.4.3 X-Ray diffraction (XRD)

X-ray crystallography is a method of determining the arrangement of atoms within a crystal, in which a beam of X-rays strikes a crystal and scatters into many different directions. X-ray diffraction is based on constructive interference of monochromatic X-rays and a crystalline sample. These X-rays are generated by a cathode ray tube, filtered to produce monochromatic radiation, collimated to

concentrate, and directed toward the sample. The interaction of the incident rays with the sample produces interference when conditions satisfy Bragg's Law:

$$2d\sin\theta = n\lambda \qquad (3.1)$$

where d is the spacing between diffracting planes, θ is the incident angle, n is any integer, and λ is the wavelength of the beam.

This law relates the wavelength of electromagnetic radiation to the diffraction angle and the lattice spacing in a crystalline sample. These diffracted X-rays are then detected, processed and counted. By scanning the sample through a range of 2θ angles, all possible diffraction directions of the lattice should be attained due to the random orientation of the material. Conversion of the diffraction peaks to d-spacings allows identification of the compound because each compound has a set of unique d-spacings. Typically, this is achieved by comparison of d-spacings with standard reference patterns.

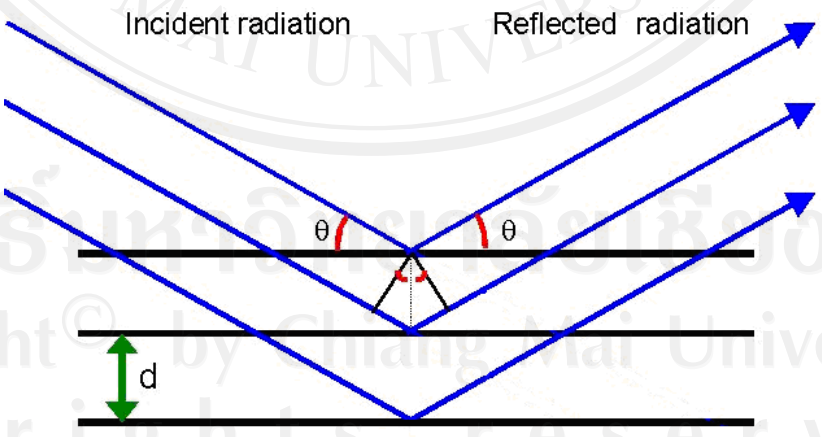

Fig. 3.14 X-Ray diffraction. **[**53**]**

In this work, room temperature X-ray diffraction studies were carried out with the PANalytical (X' pert Pro MPD, figure 3.15). The diffractrometer was operated at 40 kV with 40 mA current. Monochromatic CuK_{α} radiation of wavelength 1.54 Å was used throughout. For all measurements, a scan step mode was used with a step size of 0.0167 degree/second. Each sample was scanned for a 2θ range from 10-90 degree.

Fig. 3.15 X-ray diffractrometer.

3.4.4 UV-vis spectroscopy

Optical transmittances and absorbance were carried out in the range of 300 to 800 nm using UV-vis spectrophotometer (Hitashi U-4100).

Fig. 3.16 UV-visible spectrophotometer.

From equation 2.10, the absorption of light by the medium is quantified by

$$I = I_0 e^{-\alpha t} \qquad (2.10)$$

From the literature, there are three values of absorption coefficient.

$$\alpha_1 = \frac{1}{t}\ln\frac{(1-R)}{T} \qquad (3.3)[54],$$

$$\alpha_2 = -\ln T \qquad (3.5)[55]$$

$$\alpha_3 = \frac{(1-C)^2}{2C} \qquad (3.6)[56]$$

where t is film thickness, R is reflectance and T is transmittance.

Consider $I_0 = 1$ and I = Transmittance, so equation 2.10 can be written as

$$T = e^{-\alpha t}$$

$$\ln T = \ln e^{-\alpha t}$$

$$-\alpha t = \ln T$$

$$\alpha = (1/t)(-\ln T)$$

$$\alpha_1 = (1/t)(\ln 1/T) \qquad (3.6)$$

but there is the reflectance of light so equation 2.11 becomes

$$\alpha_1 = (1/t)\ (\ln\ (1\text{-}R)/T) \qquad (3.7)$$

Consider equation 3.7, thickness of the film has no any influence on absorbance coefficient and reflectance is very less compared to transmittance and absorbance so, eq. 3.7 can be written as $\alpha_2 = \ln 1/T = -\ln T$ (3.8)

Moreover, the absorption coefficient can be derived from the simple treatment related to the absorption transitions between direct parabolic bands (see fig. 3.17). The absorption coefficient can be expressed as

$$\alpha(h\nu) = A\sum P_{if} n_i n_f \qquad (3.9)$$

where P_{if} is the transition probability, n_i and n_f are the intensities of electrons in the initial state and of empty energy levels in the final state, respectively, and the sum is over all initial and final state.

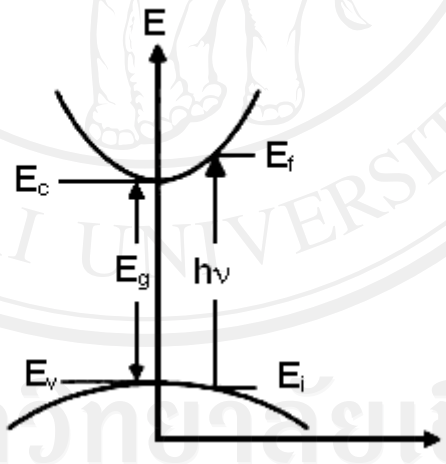

Fig. 3.17 Schematic diagram of the absorption transitions between direct parabolic bands. [57]

The energy associated with a given state is given by

$$E = \frac{\hbar^2 k^2}{2m} \qquad (3.10)$$

Thus, the electron energy (relative to E_c), $E_c = (\hbar^2 k^2)/2m_e^*$ and the hole energy (relative to E_v), $E_h = (\hbar^2 k^2)/2m_h^*$. Using this equation, for the case of the transition shown in fig. 3.16, the transition energy can be expressed as

$$h\nu = \frac{h^2 k^2}{2m_e^*} + \frac{h^2 k^2}{2m_h^*} + E_g \qquad (3.11)$$

and

$$h\nu - E_g = \frac{h^2 k^2}{2m_e^*} + \frac{h^2 k^2}{2m_h^*} = \frac{\hbar^2 k^2}{2m_r^*} \qquad (3.12)$$

where $m_r^* = m_e^* m_h^* / (m_e^* + m_h^*)$ is the reduced effective mass. The general expression for the density of state in $N(E)dE = (2\pi^2\hbar^3)^{-1}(2m^*)^{3/2}E^{1/2}dE$, and thus, for this case, the density of state can be written as

$$N(h\nu)d(h\nu) = (2\pi^2\hbar^3)^{-1}(2m_r^*)^{3/2}(h\nu - E_g)^{1/2}d(h\nu) \qquad (3.13)$$

Thus, for direct transitions between parabolic valence and conduction bands the absorption coefficient is

$$(\alpha h\nu)^2 = A(h\nu - E_g) \qquad (3.14)$$

where A is a constant, the energy gap E_g and $h\nu$ are in eV.

Energy gap of the films was estimated from the optical measurements, using equation 3.14. To determine energy gap, the variation of $(\alpha h\nu)^2$ versus $h\nu$ were plotted. Extrapolation of linear portion to the energy axis gives the band gap energy.

3.4.5 Raman spectroscopy

Raman spectroscopy is the measurement of the wavelength and intensity of inelastically scattering of monochromatic light, usually from a laser in the visible, near infrared and near ultraviolet range, from molecules. Laser can be used as the excitation source. In conventional Raman spectroscopy, visible lasers are used (e.g., Ar+, Kr+, Nd:YAG, He-Ne, diode) to stimulate the molecules to high energy "Virtual" states of excitation. A Raman photon is emitted if a molecule undergoes a transition to a higher vibrational energy state than its original state (Stokes Raman scattering), a lower energy vibrational state (Anti-Stokes Raman scattering) and the original state (Rayleigh scattering) which shown in fig. 3.18. Normally, Stokes Raman scattering has the higher intensity.

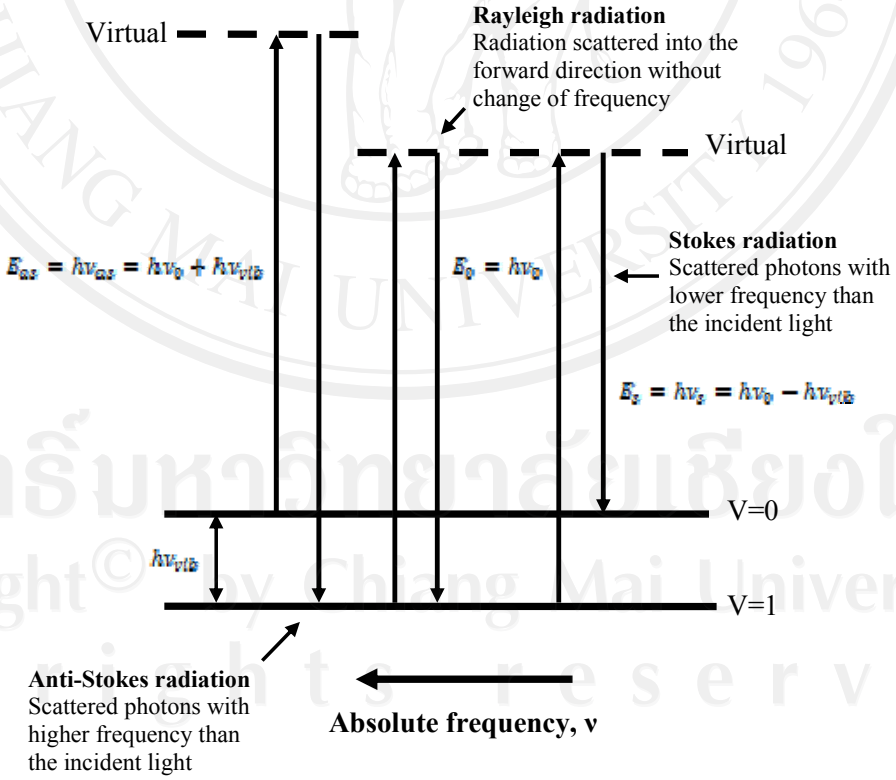

Fig. 3.18 Raman scattering [58].

In this work, the Raman spectra were obtained with a 514.5 nm argon ion laser at room temperature (Jobin Yvon Horiba T640000, fig. 3.19).

Fig 3.19 Raman spectrometer.

3.4.6 Ionoluminescence

The Ionoluminescence (IL), also known as Ion Beam Induced Luminescence (IBIL) is a luminescence phenomenon, which is caused by energetic ions penetrating matter. The light emitted under ion irradiation originates from electron transitions and recombination processes within the outer electron shells of the sample. The interactions between the ions penetrating the sample and the sample atoms lead to an energy deposition within the sample. The luminescence can be caused by the sample material itself (intrinsic) or by impurities in the sample (extrinsic), which the sample acts as a host material for the impurities.

The IL were obtained with 1.7 MV He^{2+} at room temperature (Tandetron accelerator) and Ocean Optic S2000 spectrometer (shown in fig. 3.20).

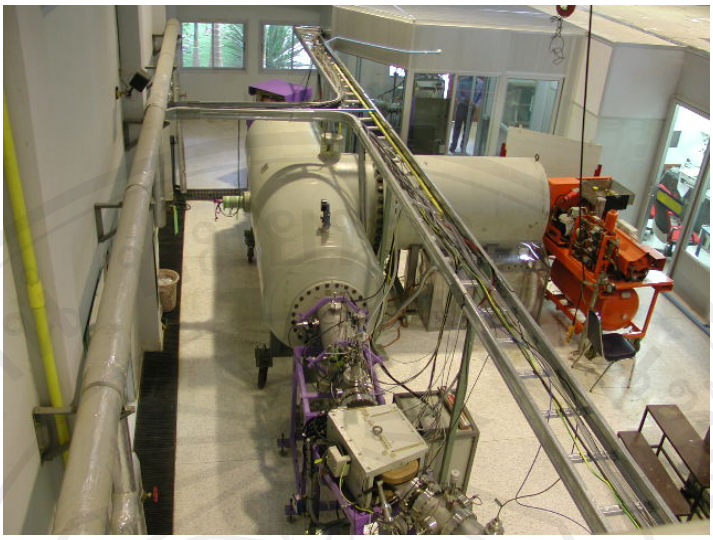

Fig. 3.20 Tandetron accelerator**.**

3.4.7 Resistivity measurement

The electrical resistances of the films were measured, at 200 °C, by coating gold as electrical contact and the film resistivities were calculated from following equation:

$$R = \frac{\rho l}{A} \qquad (3.9)$$

where R is the resistance, ρ is the film resistivity, l is 1 mm and A is cross-section area of the films.

3.4.8 Photocatalytic activity measurement

The photocatalytic properties of the obtained films using 100 μM 500 μl methyleneblue (MB) solution (Ajax Fine chem) were investigated. The films were dip in MB for 1h, under the sunlight irradiation. The absorbtion was monitored by UV-vis

spectroscopy. The absorbtion intensity of MB indicated the photocatalytic property of the films.

3.4.9 I-V curve measurement

The electroluminescent measurement schematic was shown in fig. 3.21. The silver (Ag) is electrical contact to the sparking process area and unsparked area on zinc substrate.

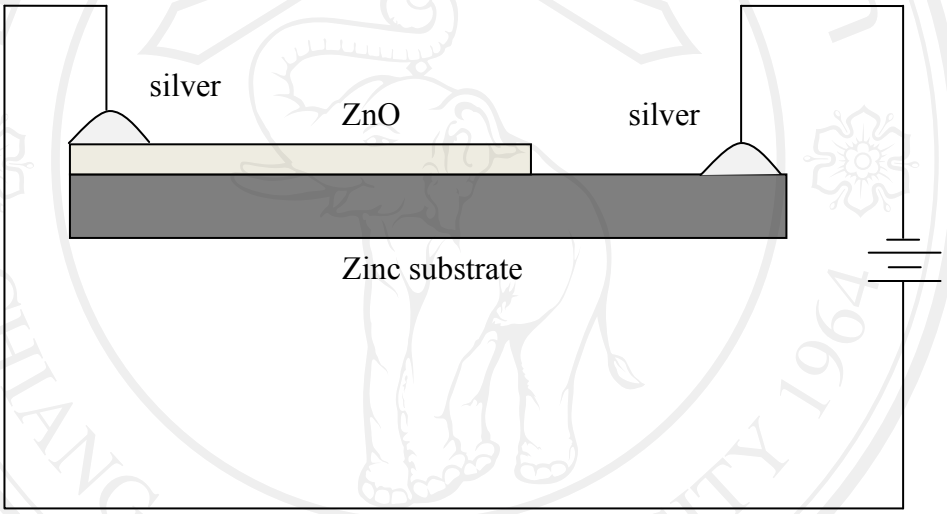

Fig 3.21 Schematic representation of an I-V curve measurement.